Evaluation of Data-Driven Respiration Gating in Continuous Bed Motion in Lung Lesions

Takeshi Nii[1], Shota Hosokawa[2], Tomoya Kotani[3], Hiroshi Domoto[1], Yasunori Nakamura[1,4], Yasutomo Tanada[1,5], Ryotaro Kondo[1], and Yasuyuki Takahashi[2]

[1]Division of Radiological Technology, Department of Medical Technology, University Hospital, Kyoto Prefectural University of Medicine, Kyoto, Japan; [2]Department of Radiation Science, Graduate School of Health Sciences, Hirosaki University, Hirosaki, Japan; [3]Department of Radiology, Graduate School of Medical Science, Kyoto Prefectural University of Medicine, Kyoto, Japan; [4]Department of Medical Physics, Graduate School of Medical Sciences, Kindai University, Osaka, Japan; and [5]Department of Quantum Medical Technology, Graduate School of Medical Sciences, Kanazawa University, Ishikawa, Japan

Respiration gating is used in PET to prevent image quality degradation due to respiratory effects. In this study, we evaluated a type of data-driven respiration gating for continuous bed motion, OncoFreeze AI, which was implemented to improve image quality and the accuracy of semiquantitative uptake values affected by respiratory motion. **Methods:** ^{18}F-FDG PET/CT was performed on 32 patients with lung lesions. Two types of respiration-gated images (OncoFreeze AI with data-driven respiration gating, device-based amplitude-based OncoFreeze with elastic motion compensation) and ungated images (static) were reconstructed. For each image, we calculated SUV and metabolic tumor volume (MTV). The improvement rate (IR) from respiration gating and the contrast-to-noise ratio (CNR), which indicates the improvement in image noise, were also calculated for these indices. IR was also calculated for the upper and lower lobes of the lung. As OncoFreeze AI assumes the presence of respiratory motion, we examined quantitative accuracy in regions where respiratory motion was not present using a [68]Ge cylinder phantom with known quantitative accuracy. **Results:** OncoFreeze and OncoFreeze AI showed similar values, with a significant increase in SUV and decrease in MTV compared with static reconstruction. OncoFreeze and OncoFreeze AI also showed similar values for IR and CNR. OncoFreeze AI increased SUV_{max} by an average of 18% and decreased MTV by an average of 25% compared with static reconstruction. From the IR results, both OncoFreeze and OncoFreeze AI showed a greater IR from static reconstruction in the lower lobe than in the upper lobe. OncoFreeze and OncoFreeze AI increased CNR by 17.9% and 18.0%, respectively, compared with static reconstruction. The quantitative accuracy of the [68]Ge phantom, assuming a region of no respiratory motion, was almost equal for the static reconstruction and OncoFreeze AI. **Conclusion:** OncoFreeze AI improved the influence of respiratory motion in the assessment of lung lesion uptake to a level comparable to that of the previously launched OncoFreeze. OncoFreeze AI provides more accurate imaging with significantly larger SUVs and smaller MTVs than static reconstruction.

Key Words: data-driven gating; lung lesions; FDG; PET/CT

In the staging, restaging, and assessment of the treatment response of lung cancer, ^{18}F-FDG PET/CT is useful (*1,2*). Evaluation of lung lesions can be influenced by respiration effects, which extend to blurred images, SUV, and metabolic tumor volume (MTV) (*3–6*). It has been reported that the respiratory motion of the lungs is greater in the lower lobe than in the upper lobe by a maximum of 6–12 cm (*7,8*). As an imaging biomarker, SUV is highly reproducible and ideal for monitoring tumor response to treatment in individual patients (*9*). But the reliability of ^{18}F-FDG PET as a way to assess treatment response is compromised if these indices, which monitor tumor responsiveness in areas affected by respiratory motion and areas not affected by respiratory motion, cannot be evaluated equivalently.

To solve these problems, a scan method with respiration gating has been developed to detect breathing motion using a device that captures respiration as a waveform and detects the expiratory phase to get a low-motion image (*10,11*). However, as only the expiration phase is used from the collected data, the scan time is extended. A mechanism was proposed that combines amplitude-based PET gating with elastic motion correction for comprehensive respiratory management (*12*). Based on the spectral analysis method developed for single-bed-position PET imaging, respiration-gated imaging can be performed with deviceless waveforms that are derived directly from PET list-mode raw data (*13,14*). Several different approaches toward deviceless waveform generation for PET have been robustly demonstrated on single-bed-position PET (*14–16*). The deviceless waveform in the multibed position was first realized by step-and-shoot collection (*17*).

OncoFreeze (Siemens) is a type of respiration gating software that combines continuous bed motion (CBM) and device- and amplitude-based PET gating with elastic motion compensation (*12*). OncoFreeze provides a new respiration gating function based on HD-Chest (Siemens) technology that does not require an increase in imaging time. OncoFreeze uses a mass-preserving optical flow to generalize respiratory motion and reconstructs the image using all breath-count data from the HD-Chest image as a reference.
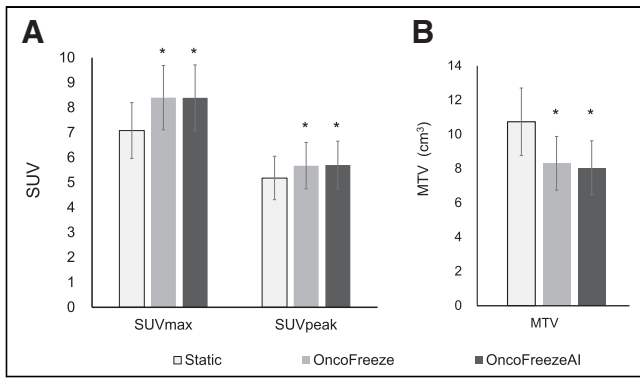
FIGURE 1. SUV$_{max}$ and SUV$_{peak}$ (A) and MTV (B) for static reconstruction, OncoFreeze, and OncoFreeze AI. *$P < 0.001$ for static reconstruction.

OncoFreeze AI (Siemens), a data-driven deviceless respiration gating system (DDG), was later created (18,19). OncoFreeze AI extracts respiratory waveforms for each patient from continuous PET data using FlowMotion technology (Siemens) and reconstructs respiration-gated images based on those respiratory waveforms. OncoFreeze AI estimates the respiratory waveform on the basis of the features of DDG and FlowMotion.

Both OncoFreeze AI and OncoFreeze are equipped on the Biograph Horizon 4R PET/CT system (Siemens) (19). The purpose of this study was to verify their usefulness in lung lesions.

MATERIALS AND METHODS

The Institutional Review Board and Ethics Committee of Kyoto Prefectural University of Medicine, Japan, approved this retrospective study (approval ERB-C-2578), and the requirement to obtain informed consent was waived. Thirty-eight lesions in 32 lung cancer patients who underwent ^{18}F-FDG respiration-gated PET/CT between January 2022 and May 2022 were included. The lesions consisted of 18 in the upper lobe, 5 in the middle lobe, and 15 in the lower lobe. The mean age of the patients was 73.7 y (range, 50–93 y), 20 were men and 12 women, their mean (±SD) body mass index was 22.28 ± 3.62, and the mean dose of ^{18}F-FDG was 202.28 ± 25.79 MBq (3.61 ± 0.65 MBq/kg).

The PET/CT examination was performed as follows. Before ^{18}F-FDG injection, the patients fasted for more than 4 h, and their blood glucose levels were confirmed to be below 200 mg/dL. Each patient received ^{18}F-FDG using an automatic injection system (Auto Dispensing Injector UG-05; Universal Giken Co. Ltd.). Imaging was performed 60 min after the ^{18}F-FDG injection using a Biograph Horizon 4R PET/CT system and using CBM at varying speeds (1.5 mm/s from the head to the pelvis and 3.5 mm/s for the lower limbs). During examination, the belt gating system (AZ-733VI; Anzai Medical, Co. Ltd.) recorded respiratory signals that were used for gating.

PET images were reconstructed using 3-dimensional ordered-subset expectation maximization coupled with point-spread-function and time-of-flight algorithms. The following clinical parameters were set: 4 iterations, 10 subsets, a postreconstruction gaussian filter of 5 mm in full width at half maximum, and a matrix of 180 × 180 pixels (pixel size, 4 mm). A low-dose CT scan was acquired for PET attenuation correction, anatomic information, and image fusion with the following scanning parameters: tube voltage, 130 kV; quality reference mAs, 90; rotation time, 0.6 s; pitch, 1.5; slice thickness, 2.0 mm; transaxial field of view, 700 mm; and matrix size, 512 × 512. At the chest, static reconstruction was performed, as well as respiration-gated reconstruction using OncoFreeze AI and OncoFreeze.

In the procedure for OncoFreeze AI, first the respiratory waveform was estimated using the change in the anterior–posterior direction from the PET data collected by FlowMotion (respiratory curve A). The PET data were then divided into 500-ms volumes and were Fourier-transformed with respect to time. Respiratory curve A was also Fourier-transformed to determine the conditions (frequency and range) to be used in the spectral analysis method. All PET data were then calculated using the spectral analysis method, and a mask was created for each voxel to compensate for the effect of respiration. The mask was applied to the temporally segmented volume data to generate a respiratory waveform (respiratory curve B), which was then normalized. Respiratory curves A and B were compared to create a deviceless respiratory waveform that matched the actual respiratory motion and allowed for respiration-gated image reconstruction (18,19).

For each reconstruction algorithm, SUV$_{max}$, SUV$_{peak}$, and MTV were measured; the threshold for MTV was set at 40% SUV$_{max}$, and the MTV unit was cm^3. The SUVs were calculated using body weight.

The improvement rate (IR) over static reconstruction with respiration gating was calculated for SUV$_{max}$, SUV$_{peak}$, and MTV.

The IR of SUV$_{max}$ (IRS$_{max}$) for OncoFreeze AI was calculated using the following formula:

$$IRS_{max} (\%) = \frac{(OncoFreeze\ AI - static)}{static} \times 100. \qquad Eq.\ 1$$

The same formula was also used to calculate the IR of SUV$_{peak}$ (IRS$_{peak}$) and the IR of MTV (IRMTV), and OncoFreeze was calculated in the same way.

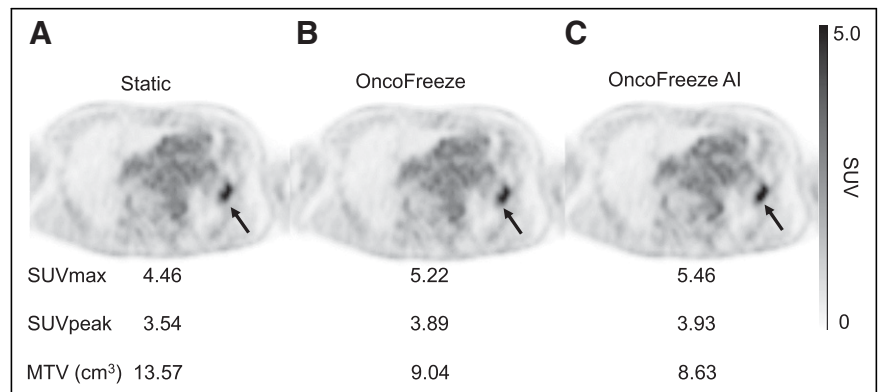SUV SD (a surrogate for image noise) was measured using a 3-cm-diameter spheric region of interest in the lung that we

FIGURE 2. A 64-y-old man with lung cancer in left upper lobe (patient height, 175.8 cm; patient weight, 76.0 kg; ^{18}F-FDG dose, 2.99 MBq/kg). Transverse PET images are shown for static reconstruction (A), OncoFreeze (B), and OncoFreeze AI (C).

	Static (A)	OncoFreeze (B)	OncoFreeze AI (C)
SUVmax	4.46	5.22	5.46
SUVpeak	3.54	3.89	3.93
MTV (cm³)	13.57	9.04	8.63

FIGURE 3. A 77-y-old woman with lung cancer in right lower lobe (patient height, 153.5 cm; patient weight, 56.7 kg; ^{18}F-FDG dose, 3.26 MBq/kg). Transverse PET images are shown for static reconstruction (A), OncoFreeze (B), and OncoFreeze AI (C).
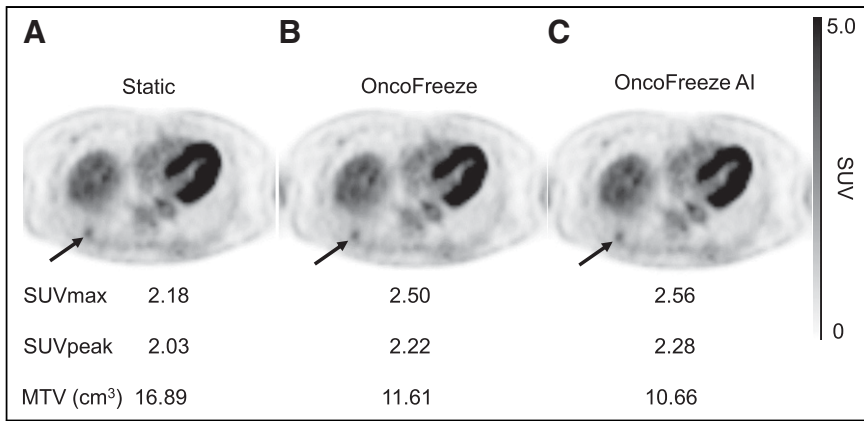
assessed to be free of disease. The contrast-to-noise ratio (CNR) for each sphere was calculated according to Equation 2 using the lesion SUV_{max}, background sphere SUV_{max}, and background sphere SUV SD:

$$CNR = \frac{(\text{lesion } SUV_{max} - \text{background sphere } SUV_{max})}{\text{background sphere SUV SD}}. \quad \text{Eq. 2}$$

The respiratory rate of the DDG-generated waveform was compared with the respiratory rate accepted by the waveform device. The accepted respiratory rate was recorded on the PET device.

^{68}Ge cylinder phantom CS-27 (Siemens), with a volume of 8,407 mL, radius of 10 cm, and radioactivity of 73.01 MBq (8.68 kBq/mL), was used to examine the quantitative accuracy in those areas where OncoFreeze AI was applied that were largely unaffected by respiratory motion. PET data were acquired at bed speeds of 0.6–3.0 mm/s (0.3 mm/s increments). A large volume of interest was constructed in the center to avoid partial-volume and edge effects, and SUV_{mean}, SUV_{max}, SUV SD, and radioactivity (Bq/mL) were calculated. These indices were determined using syngo.via (Siemens).

All statistical analyses were performed with EZR (Saitama Medical Center, Jichi Medical University), which is a graphical user interface for R (The R Foundation for Statistical Computing) designed to add statistical functions frequently used in biostatistics (20). The significance of SUV_{max}, SUV_{peak}, MTV, and CNR were determined by the Wilcoxon signed-rank test with Bonferroni adjustment. IRS_{max}, IRS_{peak}, and IRMTV were determined by the Mann–Whitney U test, and the waveform respiration rate was determined by the paired t test.

RESULTS

SUV_{max}, SUV_{peak}, and MTV calculated by OncoFreeze AI were almost the same as those calculated by OncoFreeze. Compared with static reconstruction, SUV_{max} and SUV_{peak} showed an increase and MTV a decrease (Figs. 1–3). The mean ($\pm$SE) SUV_{max} for static reconstruction, Onco Freeze, and OncoFreeze AI was 7.08 $\pm$ 1.11, 8.40 $\pm$ 1.28, and 8.39 $\pm$ 1.31, respectively; SUV_{peak} was 5.18 $\pm$ 0.86, 5.67 $\pm$ 0.93, and 5.70 $\pm$ 0.95, respectively; and MTV was 10.73 $\pm$ 1.96, 8.31 $\pm$ 1.56, and 8.05 $\pm$ 1.51, respectively. The SUV_{max}, SUV_{peak}, and MTV of OncoFreeze AI and OncoFreeze correlated well (Fig. 4).

IRS_{max}, which represents the improvement in SUV_{max}, was 18.3% $\pm$ 2.6% for OncoFreeze and 17.9% $\pm$ 2.2% for OncoFreeze AI. IRS_{peak} was 9.7% $\pm$ 1.3% for OncoFreeze and 9.6% $\pm$ 1.3% for OncoFreeze AI. IRMTV was -24.2% $\pm$ 3.2% for OncoFreeze and -25.5% $\pm$ 2.9% for OncoFreeze AI. IRS_{max} in the upper and lower lobes was 12.0% $\pm$ 2.2% and 26.7% $\pm$ 5.2%, respectively, for Onco Freeze and 13.9% $\pm$ 2.2% and 23.8% $\pm$ 4.3%, respectively, for OncoFreeze AI. IRS_{peak} in the upper and lower lobes was 7.5% $\pm$ 1.0% and 13.3% $\pm$ 2.9%, respectively, for Onco Freeze and 7.4% $\pm$ 1.1% and 12.9% $\pm$ 2.7%, respectively, for OncoFreeze AI. IRMTV in the upper and lower lobes was -17.2% $\pm$ 3.9% and -33.7% $\pm$ 5.7%, respectively, for OncoFreeze and -22.1% $\pm$ 3.8% and -32.1% $\pm$ 5.2%, respectively, for OncoFreeze AI (Figs. 5 and 6). Only the IRS_{max} of OncoFreeze differed significantly between the upper and lower lobes ($P = 0.0273$); otherwise, there were no significant differences between the upper and lower lobes for either OncoFreeze or OncoFreeze AI.

CNR was significantly higher for OncoFreeze and OncoFreeze AI than for static reconstruction (Fig. 7). The percentage increases for CNR in comparison to static reconstruction for OncoFreeze and OncoFreeze AI were 17.9% and 18.0%, respectively. In OncoFreeze AI and OncoFreeze, the number of breaths in the generated waveform was expressed as counts. The respiratory rate of the DDG-generated waveform (OncoFreeze AI) was 223.7 $\pm$ 31.2 counts, and the respiratory rate accepted by the waveform device (OncoFreeze) was 218.0 $\pm$ 52.5 counts; this difference was not significant ($P = 0.602$). Statistical significance was set as $P < 0.05$. The
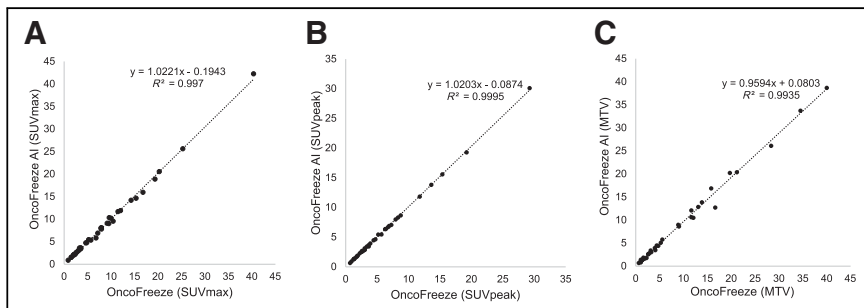

FIGURE 4. Correlation of OncoFreeze and OncoFreeze AI for SUV_{max} (A), SUV_{peak} (B), and MTV (C).
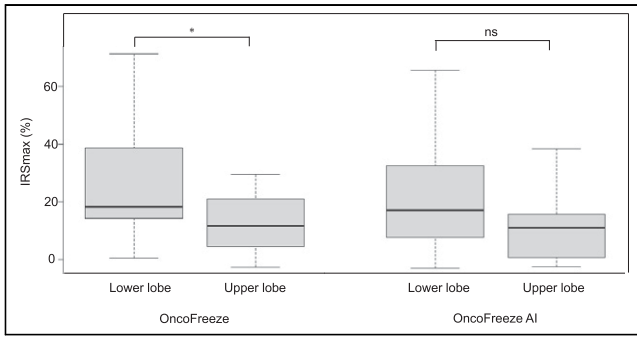
FIGURE 5. IRS_{max} from static reconstruction to OncoFreeze and OncoFreeze AI for 18 upper-lobe and 15 lower-lobe lesions. ns = not statistically significant. *P = 0.0273.

correlation of the accepted respiratory rate was $y = 1.31x - 76.57$, with $R^2 = 0.61$ (x, OncoFreeze AI; y, Onco Freeze).

The effect of OncoFreeze AI on quantitative accuracy was examined using a ^{68}Ge cylinder phantom, assuming a region of unchanged counts, and the SUV_{mean} of the volume of interest was 1.04 for both static reconstruction and OncoFreeze AI, regardless of bed speed. On the other hand, SUV_{max} for both static reconstruction and OncoFreeze AI increased slightly with increasing bed speed. SUV_{max} was slightly higher for OncoFreeze AI than for static reconstruction. The SUV_{max} of OncoFreeze AI, when the SUV_{max} of static reconstruction was set to 1, averaged 1.05 ± 0.02, showing little deviation from the increase in the SUV_{max} of static reconstruction with increasing bed speed. The radioactivity at the acquisition date, calculated from the radioactivity at the assay date, was 8.68 kBq/mL, and the mean radioactivity of static reconstruction and OncoFreeze AI was 9.06 ± 0.01 and 9.02 ± 0.02 kBq/mL, respectively (Table 1).

DISCUSSION

We compared OncoFreeze AI, a deviceless respiration gating system for CBM imaging, with OncoFreeze, a device-based system, on the Biograph Horizon, a popular commercially available general-purpose PET/CT machine. Reports so far have not investigated use on popular PET/CT systems and
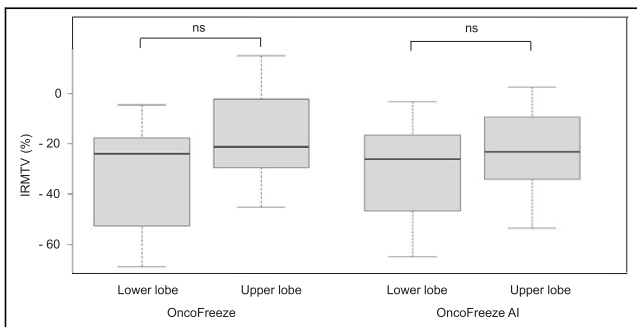
instead have focused on the high-end Biograph mCT (Siemens) and a semiconductor PET machine, Biograph Vision (Siemens) (18,21). In this study, we found that on the Biograph Horizon, OncoFreeze AI and OncoFreeze had the same SUV_{max}, SUV_{peak}, and MTV in lung lesions (Fig. 4).

Respiratory motion is greater in the lower lobe than in the upper lobe (4). IRS_{max}, IRS_{peak}, and IRMTV showed a trend toward a greater correction effect on respiratory motion in the lower lobe than in the upper lobe. However, there was no significant difference in correction effect between the upper and lower lobes, except for IRS_{max} in OncoFreeze ($P = 0.0273$) (Figs. 5 and 6). Robin et al. reported a greater increase in SUV and decrease in MTV in the lower lobe than in the upper lobe because of the correction effect of respiratory motion on amplitude-based respiration-gated HD-Chest imaging (6). In the present study, the same trend was observed for both OncoFreeze and OncoFreeze AI.

Meier et al. used CNR as a metric to capture both SUV_{max} and noise. Their study reported a decrease in CNR with correction methodologies that use decreasing amounts of PET data; however, in lung lesions, the elastic motion deblurring algorithm improved the CNR of the lesion by 17.8%, with the least increase in image noise (22). In the present study, OncoFreeze and OncoFreeze AI, which did not involve a decrease in PET data, showed a significant increase in CNR (17.9% and 18.0%, respectively). The fact that the respiratory rate generated by OncoFreeze AI, which generates respiratory waveforms without a device, was not significantly different from the respiratory rate measured by the device also indicates the usefulness of OncoFreeze AI.

Since OncoFreeze AI is a deviceless method, the waveforms generated are completely dependent on the acquired PET data. To extract respiratory signals, respiratory motion must be present in the PET data (19). Therefore, using a ^{68}Ge cylinder phantom, we verified the accuracy of quantification in a region where no respiratory motion was assumed, and we found that SUV_{mean} and quantification accuracy were

FIGURE 6. IRMTV from static reconstruction to OncoFreeze and OncoFreeze AI for 18 upper-lobe and 15 lower-lobe lesions. ns = not statistically significant.
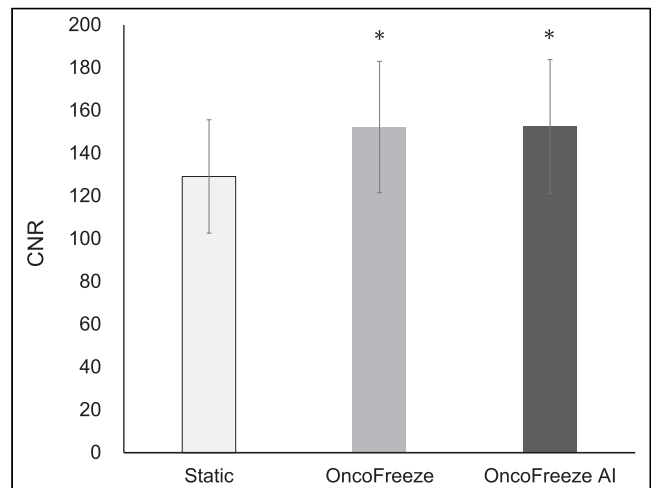

FIGURE 7. Static reconstruction, OncoFreeze, and OncoFreeze AI in CNR. *$P < 0.001$ for static reconstruction.

TABLE 1
Relationship Between Bed Motion Speed, Radioactivity Concentration, and SUV in ^{68}Ge Cylinder Phantom

Bed speed (mm/s)	Activity (kBq/mL)		SUV_{mean}		SUV SD		SUV_{max}	
	Static	OncoFreeze AI	Static	OncoFreeze AI	Static	OncoFreeze AI	Static	OncoFreeze AI
0.6	9.05	9.03	1.04	1.04	0.04	0.04	1.22	1.28
0.9	9.06	9.02	1.04	1.04	0.05	0.06	1.25	1.33
1.2	9.05	9.02	1.04	1.04	0.05	0.06	1.31	1.39
1.5	9.07	9.04	1.04	1.04	0.06	0.07	1.34	1.38
1.8	9.06	9.02	1.04	1.04	0.07	0.08	1.44	1.50
2.1	9.08	9.04	1.05	1.04	0.07	0.09	1.44	1.50
2.4	9.06	9.00	1.04	1.04	0.08	0.10	1.42	1.55
2.7	9.07	9.01	1.04	1.04	0.08	0.10	1.47	1.52
3.0	9.07	8.99	1.04	1.04	0.09	0.10	1.43	1.59

comparable to those of static reconstruction. SUV_{max} was slightly higher for OncoFreeze AI than for static reconstruction, but the change in SUV_{max} with increasing bed speed was the same for static reconstruction and OncoFreeze AI (Table 1). These results indicate that OncoFreeze AI reduced the effect of respiratory motion without compromising quantitative accuracy in the absence of respiratory motion.

There were some limitations to our study. Though the image quality and other semiquantitative parameters improved, clinical impact on patient management needs further evaluation. The present technique not only improved detection of lung lesions but also may improve detection of subdiaphragmatic hepatic lesions, which is a potential additional advantage but not examined in the present study.

One of the features of PET/CT with the CBM mechanism, such as on the Biograph Horizon, is the whole-body dynamic imaging function. At present, dynamic images from whole-body dynamic imaging cannot be combined with OncoFreeze AI; however, when this capability is realized, it will be useful (23–27). OncoFreeze AI eliminates the need to attach the device to the patient, leading to shorter examination times for the patient and reduced radiation exposure for the operator. Respiration-gated reconstruction that takes into account the effects of respiratory motion is expected to significantly contribute to SUV and harmonization, which are widely used in clinical studies of lung cancer (28,29).

CONCLUSION

OncoFreeze AI, which does not require a device, can calculate SUVs and metabolic volumes comparable to those of OncoFreeze, which uses a device to measure respiratory motion. Compared with static reconstruction, OncoFreeze AI provides more accurate lung lesion images with significantly larger SUVs and smaller metabolic volumes.

DISCLOSURE

No potential conflict of interest relevant to this article was reported.

KEY POINTS

QUESTION: Is a commercialized DDG application useful for evaluating lung lesion uptake in CBM ^{18}F-FDG PET?

PERTINENT FINDINGS: Data-driven respiration gating was performed on 38 lung lesions in a CBM ^{18}F-FDG PET study and significantly increased SUV and decreased MTV compared with no gating. Although data-driven deviceless respiration-gated reconstruction assumes the presence of respiratory motion, the phantom test results did not impair quantification in regions where respiratory motion was absent.

IMPLICATIONS FOR PATIENT CARE: DDG reconstruction for evaluation of lung lesions in CBM FDG PET can properly evaluate ^{18}F-FDG uptake.

REFERENCES

1. Brink1 I, Schumacher T, Mix1 M, et al. Impact of ^{18}F-FDG-PET on the primary staging of small cell lung cancer. *Eur J Nucl Med Mol Imaging.* 2004; 31:1614–20.
2. Verhagen AF, Bootsma GP, Tjan-Heijnenc VCG, et al. FDG-PET in staging lung cancer: how does it change the algorithm? *Lung Cancer.* 2004;44:175–181.
3. García Vicente AM, Soriano Castrejón AM, Talavera Rubio MP, et al. ^{18}F-FDG PET-CT respiratory gating in characterization of pulmonary lesions: approximation towards clinical indications. *Ann Nucl Med.* 2010;24:207–214.
4. Lupi A, Zaroccolo M, Salgarello M, Malfatti V, Zanco P. The effect of ^{18}F-FDG-PET/CT respiratory gating on detected metabolic activity in lung lesions. *Ann Nucl Med.* 2009;23:191–196.
5. Callahan J, Binns D, Dunn L, Kron T. Motion effects on SUV and lesion volume in 3D and 4D PET scanning. *Australas Phys Eng Sci Med.* 2011;34:489–495.

6. Robin P, Bourhis D, Bernard B, et al. Feasibility of systematic respiratory-gated acquisition in unselected patients referred for ^{18}F-fluorodeoxyglucose positron emission tomography/computed tomography. *Front Med (Lausanne)*. 2018;5:36.

7. Seppenwoolde Y, Shirato H, Kitamura K, et al. Precise and real-time measurement of 3D tumor motion in lung due to breathing and heartbeat, measured during radiotherapy. *Int J Radiat Oncol Biol Phys*. 2002;53:822–834.

8. Knybel L, Cvek J, Molenda L, Stieberova N, Feltl D. Analysis of lung tumor motion in a large sample: patterns and factors influencing precise delineation of internal target volume. *Int J Radiat Oncol Biol Phys*. 2016;96:751–758.

9. Lodge MA. Repeatability of SUV in oncologic ^{18}F-FDG PET. *J Nucl Med*. 2017;58:523–532.

10. Nehmeh SA, Erdi YE, Ling CC, Rosenzweig KE, Schoder H, Larson SM. Effect of respiratory gating on quantifying PET images of lung cancer. *J Nucl Med*. 2002;43:876–881.

11. Werner MK, Parker JA, Kolodny GM, English JR, Palmer MR. Respiratory gating enhances imaging of pulmonary nodules and measurement of tracer uptake in FDG PET/CT. *AJR*. 2009;193:1640–1645.

12. Pösse S, Büther F, Mannweiler D, et al. Comparison of two elastic motion correction approaches for whole-body PET/CT: motion deblurring vs gate-to-gate motion correction. *EJNMMI Phys*. 2020;7:19.

13. Walker MD, Morgan AJ, Bradley KM, McGowan DR. Data-driven respiratory gating outperforms device-based gating for clinical ^{18}F-FDG PET/CT. *J Nucl Med*. 2020;61:1678–1683.

14. Schleyer PJ, O'Doherty MJ, Barrington SF, Marsden PK. Retrospective data-driven respiratory gating for PET/CT. *Phys Med Biol*. 2009;54:1935–1950.

15. Kesner AL, Bundschuh RA, Detorie NC, et al. Respiratory gated PET derived in a fully automated manner from raw PET data. *IEEE Trans Nucl Sci*. 2009;56:677–686.

16. Büther F, Dawood M, Stegger L, et al. List mode–driven cardiac and respiratory gating in PET. *J Nucl Med*. 2009;50:674–681.

17. Walker MD, Morgan AJ, Bradley KM, McGowan DR. Evaluation of data-driven respiratory gating waveforms for clinical PET imaging. *EJNMMI Res*. 2019;9:1.

18. Büther F, Jones J, Seifert R, Stegger L, Schleyer P, Schäfers M. Clinical evaluation of a data-driven respiratory gating algorithm for whole-body PET with continuous bed motion. *J Nucl Med*. 2020;61:1520–1527.

19. Jones J, Hamill J, Fuerst S, Schleyer P, Hong I. *White Paper: OncoFreeze AI Deviceless Motion Management for PET Imaging*. Siemens Healthcare GmbH; 2020.

20. Kanda Y. Investigation of the freely available easy-to-use software 'EZR' for medical statistics. *Bone Marrow Transplant*. 2013;48:452–458.

21. Dias AH, Schleyer P, Vendelbo MH, Hjorthaug K, Gormsen LC, Munk OL. Clinical feasibility and impact of data-driven respiratory motion compensation studied in 200 whole-body ^{18}F-FDG PET/CT scans. *EJNMMI Res*. 2022;12:16.

22. Meier1 JG, Wu CC, Cuellar SLB, et al. Evaluation of a novel elastic respiratory motion correction algorithm on quantification and image quality in abdominothoracic PET/CT. *J Nucl Med*. 2019;60:279–284.

23. Nishimura M, Tamaki N, Matsushima S, et al. Dynamic whole-body ^{18}F-FDG PET for differentiating abnormal lesions from physiological uptake. *Eur J Nucl Med Mol Imaging*. 2020;47:2293–2300.

24. Kotani T, Nishimura M, Tamaki N, et al. Comparison between dynamic whole-body FDG-PET and early-delayed imaging for the assessment of motion in focal uptake in colorectal area. *Ann Nucl Med*. 2021;35:1305–1311.

25. Nii T, Hosokawa S, Shirako K, et al. Achievements of true whole-body imaging using a faster acquisition of the lower extremities in variable-speed continuous bed motion. *Radiol Phys Technol*. 2021;14:373–380.

26. Naganawa M, Gallezot JD, Shah V, et al. Assessment of population-based input functions for Patlak imaging of whole body dynamic ^{18}F-FDG PET. *EJNMMI Phys*. 2020;7:67.

27. Osborne DR, Acuff S. Whole-body dynamic imaging with continuous bed motion PET/CT. *Nucl Med Commun*. 2016;37:428–431.

28. Berghmans T, Dusart M, Paesmans M, et al. Primary tumor standardized uptake value (SUVmax) measured on fluorodeoxyglucose positron emission tomography (FDG-PET) is of prognostic value for survival in non-small cell lung cancer (NSCLC): a systematic review and meta-analysis (MA) by the European lung cancer working party for the IASLC lung cancer staging project. *J Thorac Oncol*. 2008;3:6–12.

29. Houdu B, Lasnon C, Licaj I, et al. Why harmonization is needed when using FDG PET/CT as a prognosticator: demonstration with EARL-compliant SUV as an independent prognostic factor in lung cancer. *Eur J Nucl Med Mol Imaging*. 2019;46:421–428.